






## Open Archive Toulouse Archive Ouverte (OATAO)

OATAO is an open access repository that collects the work of Toulouse researchers and makes it freely available over the web where possible

This is an author's version published in: <http://oatao.univ-toulouse.fr/24460>

**Official URL:** <https://doi.org/10.1149/2.0071602jes>

### To cite this version:

Berne, Clément  and Andrieu, Eric  and Reby, Jean and Sobrino, Jean-Michel and Blanc, Christine  *Dissolution Kinetics of  $\alpha,\beta'$ -Brass in Basic NaNO<sub>3</sub> Solutions*. (2016) *Journal of The Electrochemical Society*, 163 (2). C7-C15. ISSN 0013-4651

Any correspondence concerning this service should be sent to the repository administrator: [tech-oatao@listes-diff.inp-toulouse.fr](mailto:tech-oatao@listes-diff.inp-toulouse.fr)

# Dissolution Kinetics of $\alpha,\beta'$ -Brass in Basic $\text{NaNO}_3$ Solutions

C. Berne,<sup>a,b,c,\*</sup> E. Andrieu,<sup>b</sup> J. Reby,<sup>c</sup> J-M. Sobrino,<sup>d</sup> and C. Blanc<sup>b,\*\*,z</sup>

<sup>a</sup>Joint Laboratory CETIMAT, CETIM – CIRIMAT, 31030 Toulouse Cedex 4, France

<sup>b</sup>Université de Toulouse, CIRIMAT, UPS/INPT/CNRS, Equipe MEMO, ENSIACET, 31030 Toulouse Cedex 4, France

<sup>c</sup>CETIM, Pôle Matériaux Métalliques et Surface, 44326 Nantes Cedex 3, France

<sup>d</sup>CETIM, Pôle Matériaux Métalliques et Surface, 60304 Senlis Cedex, France

Corrosion tests at a constant anodic potential, referred to as dissolution tests, were performed to determine the dissolution kinetics of an  $\alpha,\beta'$ -brass CuZn40Pb2 (CW617N) in a basic nitrate solution with and without mechanical loading. The corrosion behavior of the  $\alpha,\beta'$ -brass was characterized by a two-step mechanism, with an initiation step for which the simultaneous dissolution of all the alloying elements of the  $\beta'$  phase occurred only and a propagation step including at first, the afore-mentioned simultaneous dissolution process before a critical time  $t_c$  and then, both simultaneous dissolution and dezincification of the  $\beta'$  phase after  $t_c$ . The pH and Cu concentration of the electrolyte near the brass surface were determined to be two of the major factors influencing the occurrence of the dezincification process. The dezincification of the  $\beta'$  phase extended in depth by a percolation dissolution mechanism. Mechanical loading during the dissolution tests was observed to largely influence the dezincification process. It was assumed to open or close the pores present in the dezincified  $\beta'$  phase, which promoted or slowed down the dezincification mechanism depending on the sign of the stress.

[DOI: [10.1149/2.0071602jes](https://doi.org/10.1149/2.0071602jes)]

In various corrosive environments,  $\alpha,\beta'$ -brasses are believed to be susceptible to simultaneous dissolution (Cu, Zn) and/or selective dissolution (Zn, dezincification) processes. These phenomena are expected to play a major role during the first stages (incubation and initiation) of stress corrosion cracking (SCC) damage,<sup>1</sup> leading to rupture, that have been observed on gas network components in service. In this framework, it is of interest to develop accelerated tests to evaluate the susceptibility to corrosion and SCC of  $\alpha,\beta'$ -brasses, however the development of these accelerated tests requires a good knowledge of brass dissolution mechanisms. Abundant literature can be found for  $\alpha$ -brass, for example in nitrite solutions<sup>2-11</sup> but not for  $\alpha,\beta'$ -brasses.<sup>12-15</sup> In a previous study,<sup>16</sup> the electrochemical behavior of an  $\alpha,\beta'$ -brass CuZn40Pb2 (CW617N) was studied in basic nitrate solutions with various basic pHs and nitrate ion concentrations. This specific alloy, CW617N, used principally for its good malleability and machinability (related to the Pb amount) and resistance to corrosion, is principally studied for the development of water taps.<sup>17-19</sup> The  $\text{NaNO}_3$  solution was selected on the basis of a literature review on  $\alpha$ -brass.<sup>20</sup> In the literature, the solutions that are most often used are ammonia,<sup>15,21</sup> sulfuric acid,<sup>22</sup> and nitrite solutions<sup>10</sup> but, according to Fernandez et al.,<sup>20</sup> the nitrate ion is far more stable in low pH solution than the nitrite ion. Because the present study was a first step to develop an accelerated SCC test, the nitrite ion was avoided due to its instability in the acid solution that is expected to exist inside a stress corrosion crack. Ammonia solutions, widely used for testing brass corrosion resistance, were also excluded due to the lack of reproducibility of SCC tests performed in this environment. The results from a previous study<sup>16</sup> showed that, in all the chosen experimental conditions, corrosion at the open circuit potential proceeded by the galvanic coupling of the  $\alpha$  and  $\beta'$  phases, leading to a surface dezincification of the  $\beta'$  phase. The extent of the dezincification was affected by the presence of lead in the alloy but the pH was the major parameter. During polarization tests, a pseudo-passive or a passive stage followed by a pseudo-passivity or a passivity breakdown was observed; the corrosion phenomena mainly involved copper and zinc dissolution from the  $\beta'$  phase. At pH 11, a  $\text{Cu}_2\text{O}/\text{PbO}$  layer was efficient in achieving passivity of the brass, whereas for potentials higher than 0.03 V/SCE, local dissolution of the  $\beta'$  phase was observed. At pH 12, a  $\text{Cu}(\text{OH})_2$ -rich surface layer was formed in the pseudo-passivity range; it was not protective enough, and complete dissolution of the  $\beta'$

phase was observed for potentials higher than 0.115 V/SCE leading to the removal of lead particles. The results were consistent with those of Heidersbach and Verink<sup>23</sup> who proposed that preferential dissolution of Zn occurred at low potentials, while for higher potentials, both copper and Zn dissolved with or without copper re-deposition depending on the potential value. They were also in good agreement with other authors<sup>20,24-25</sup> who showed that the precipitation of lead based compounds on the surface of the brass, for potentials higher than the corrosion potential, decreases the extent of corrosion attack. Results from a previous study<sup>16</sup> brought a new insight into the chemical composition of the surface layer depending on the pH and the applied potential. However, tests performed in this previous study were short and knowledge of the dissolution mechanisms and kinetics of  $\alpha,\beta'$ -brasses during long tests is important to understand their SCC behavior. Furthermore, in the framework of the development of an SCC test, it was of interest to determine the influence of a mechanical loading on the dissolution mechanism and kinetics. Among the mechanisms proposed in literature<sup>22,26-29</sup> that could be used to explain the dissolution behavior of  $\alpha,\beta'$ -brasses for long dissolution tests, a volume diffusion mechanism was discussed by Pickering,<sup>26-28</sup> Sieradzki et al.<sup>30-33</sup> proposed another model called “percolation dissolution” while also discussing the major dealloying mechanisms in a recent paper.<sup>34</sup>

In the present study, dissolution tests in a basic  $\text{NaNO}_3$  solution were performed for the  $\alpha,\beta'$ -brass CuZn40Pb2 to contribute to a better understanding of the dissolution processes and kinetics of  $\alpha,\beta'$ -brass under a constant anodic potential and under specific mechanical loading in the framework of the development of accelerated SCC tests. Measurements of both the dissolution depths and the weight loss, chemical analyses of the corroded materials, the corrosion products and the solutions were performed to quantify the dissolution processes. The discussion focuses on the dissolution mechanism with reference to the  $\alpha$ -brass dissolution processes proposed in the literature.<sup>1-2,26-35</sup>

## Experimental

**Material.**— The material used is the  $\alpha,\beta'$ -brass CuZn40Pb2 (CW617N) removed from extruded rods, as reported in a previous study.<sup>16</sup> Its chemical composition obtained from inductively coupled plasma (ICP) measurements is presented in Table I. Its microstructure was characterized by using optical microscope (OM) observations after abrading, polishing and etching the brass sample surface using Klemm II solution (24 g  $\text{Na}_2\text{S}_2\text{O}_3$ , 5 g  $\text{K}_2\text{S}_2\text{O}_5$ , 50 mL  $\text{H}_2\text{O}$ ) for 9 minutes.

\*Electrochemical Society Student Member.

\*\*Electrochemical Society Active Member.

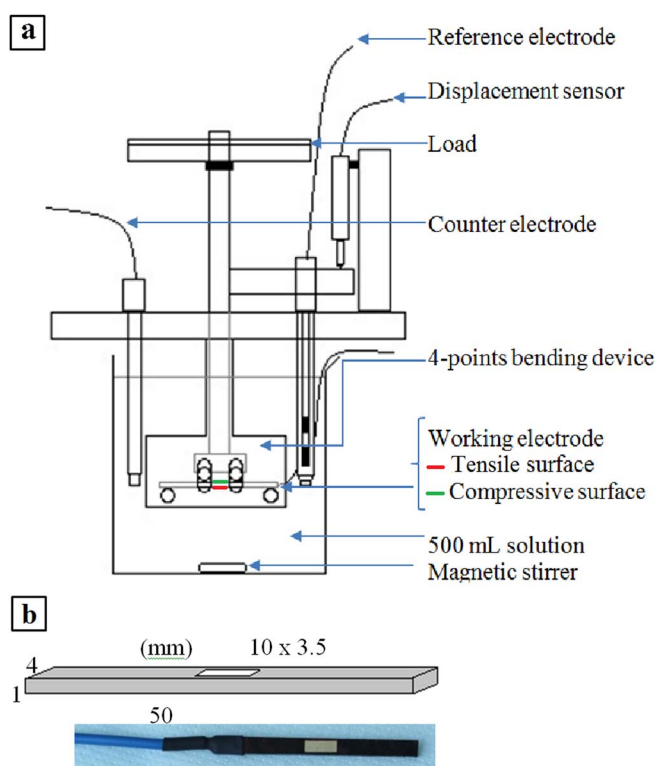
<sup>z</sup>E-mail: [christine.blanc@ensiacet.fr](mailto:christine.blanc@ensiacet.fr)

**Table I. Chemical composition of the  $\alpha,\beta'$ -brass CuZn40Pb2 (CW617N) and chemical composition of the  $\alpha$  and  $\beta'$  phases.**

Elements	Inductively coupled plasma atomic emission spectroscopy		Electron microprobe			
	Extruded rod		$\alpha$ Phase		$\beta'$ Phase	
	wt %	at %	wt %	at %	wt %	at %
Zn	38.35	38.20	36.40	35.80	44.10	43.80
Al	0.008	0.019	0.008	0.02	0.01	0.03
Ni	0.051	0.057	0.12	0.13	-	0.10
Fe	0.205	0.239	0.26	0.30	0.08	0.09
Mn	0.004	0.005	-	-	-	-
Sn	0.150	0.082	0.08	0.05	0.48	0.26
Pb	1.875	0.589	0	0	0	0
Si	0.001	0.002	-	-	-	-
Cu	59.35	60.81	63.10	63.70	54.10	55.30

**Dissolution tests.**— A dissolution test consisted of the immersion of the sample in a nitrate solution with an anodic potential applied on the sample after 15 minutes of immersion at OCP. The duration of the dissolution tests was between 2 h and 48 h. Based on the results from the previous study,<sup>16</sup> a 0.5 M  $\text{NaNO}_3$  solution with a pH adjusted to 11 was used. The reference conditions corresponded to dissolution tests performed in the solution without mechanical loading and under an anodic potential equal to 0.05 V/SCE, i.e., a potential after the passivity breakdown, as identified in the previous study.<sup>16</sup> Experiments were performed with a standard device composed of a potentiostat connected to a reference electrode (Saturated Calomel Electrode), a counter electrode (platinum) and a working electrode composed of an  $\alpha,\beta'$ -brass sample. The surface exposed to the electrolyte corresponded to the plane perpendicular to the extrusion direction. For the major parts of the dissolution tests, a surface area of 0.2  $\text{cm}^2$  (surface/volume ratio =  $S/V = 6.7 \times 10^{-4} \text{ cm}^2/\text{mL}$ ) was selected by using a varnish. The sample surface was polished with 4000 grit SiC paper before the experiment. Tests were performed with 300 mL of the solution that was open to the air, moderately stirred with a magnetic stirrer and maintained at  $23.5 \pm 2^\circ\text{C}$  using a thermostatically-controlled water-bath. A few experiments were performed with 0.02  $\text{cm}^2$  and 4  $\text{cm}^2$  of the surface exposed to 300 mL of the solution (respectively  $S/V = 6.7 \times 10^{-5} \text{ cm}^2/\text{mL}$  and  $1.3 \times 10^{-2} \text{ cm}^2/\text{mL}$ ) to study the influence of the  $S/V$  ratio on the dissolution kinetics.

To better understand the effect of mechanical loading on the anodic dissolution of  $\alpha,\beta'$ -brass CuZn40Pb2, some dissolution tests were performed while applying a mechanical load using a bending device (Figure 1a), allowing for the specimen to be completely immersed in 500 mL of the electrolyte solution. The geometry of the tested specimen is presented in Figure 1b. The stress was perpendicular to the extrusion direction. These conditions were chosen to correspond to the most rigorous requirements according to preliminary tests, not presented here. The surface, either under tensile or compressive loading (Figure 1a), was exposed to the electrolyte using a protective varnish on the non-exposed surface. In each case, the surface exposed to the electrolyte corresponded to a zone in a rectangular shape ( $10 \times 3.5 \text{ mm}^2$ ; surface/volume ratio =  $7.10^{-4} \text{ cm}^2/\text{mL}$ , close to previous  $S/V$  values of  $6.7 \times 10^{-4} \text{ cm}^2/\text{mL}$ ) in the center of the specimen between the two interior support rollers. The same standard device used in the dissolution tests, without mechanical loading, was used here (Potentiostat, 3 electrodes, magnetic stirring, and thermostatically controlled water-bath). An initial maximal stress of 140 MPa was applied to achieve 70% of the yield strength at 0.2% of strain at the surface of the specimen, which was previously determined by traction tests at  $10^{-3} \text{ s}^{-1}$  and found to be 205 MPa. The dissolution test was then performed at constant mechanical loading. Displacements during the tests were followed with a sensor (Keyence-GT2-H12K). It is worth noting that some dissolution tests, at the reference conditions, were performed with samples placed on the bending device without

**Figure 1.** (a) Schematic of the bending device used to determine the influence of mechanical loading on the dissolution kinetics. (b) Geometry of the specimen.

applying a mechanical loading to allow comparison between results with and without a mechanical loading by eliminating the effects of the bending device. Furthermore, a preliminary study showed that the OCP values measured for 15 minutes in a 0.5 M nitrate solution at pH 11 for a surface under compressive or tensile loading were similar to those measured for a non-loaded surface; current-potential curves plotted at a scan rate of  $0.070 \text{ mV}\cdot\text{s}^{-1}$  were similar for the loaded and non-loaded surfaces.

The experiments performed are described in Table II.

**Characterization of the corrosion damage.**— After dissolution tests at a constant potential were completed, cross-sections of the corroded material were prepared. They were observed using an optical microscope (NIKON) to measure the dissolution depths, and more detailed observations were performed by a scanning electron microscope (SEM, LEO435VP LEO) coupled with an Energy-dispersive

**Table II. Description of the experimental conditions for the dissolution tests.**

	Potential applied (V/SCE)	pH	Nitrate ion concentration (M)	S/V cm <sup>2</sup> /mL	Mechanical loading (MPa)
Reference conditions	0.05	11	0.5	$6.7 \times 10^{-4}$	0
S/V effect	0.05	11	0.5	$6.7 \times 10^{-5}$	0
	0.05	11	0.5	$1.3 \times 10^{-2}$	0
Mechanical loading effect	0.05	11	0.5	$7 \times 10^{-4}$	140 (at the surface)
	0.05	11	0.5	$7 \times 10^{-4}$	0

X-ray spectrometer (EDS) for chemical analyses. For the dissolution depths, 5 measurements were performed for one sample all along the center of the exposed zone. For each experimental condition, 3 samples were analyzed for reproducibility. Each point on the dissolution curve corresponds to a mean value obtained from 15 measurements (i.e., 5 measurements for one sample  $\times$  3 samples). Error bars on the curves take into account the 15 measurements. For each curve, data obtained for different durations correspond to different samples. Weight loss measurements were also performed using a precision balance: after the dissolution tests at a constant potential, the samples were rinsed using distilled water to remove the major part of the corrosion products, and then air-dried. They were weighed and their weight was compared to the weight measured before the dissolution tests. Corrosive solution analyses were performed using inductively coupled plasma atomic emission spectroscopy (ICP-AES - Ultima 2 Horiba). Analyses were performed after rinsing the working electrode and reference electrode with distilled water, as well as dissolving the corrosion products deposited on the platinum electrode with dilute nitric acid leading to a solution called rinsing solution. The rinsing solution and the electrolyte used for the dissolution tests were mixed and the corrosion products present in the mixture were dissolved with dilute nitric acid to perform ICP analyses. X-ray diffraction (XRD) experiments were also performed to analyze the corrosion products removed from the solution. A 2- $\theta$  scan was performed from 20° to 70° using Cu K- $\alpha$  radiation and SEIFERT-3000TT equipment.

## Results

**Microstructure.**— The metallurgical state of the brass was described in a previous study.<sup>16</sup> It corresponded to that of the center of a 65 mm diameter extruded rod (Figure 2). The  $\alpha$  phase (64 at. % Cu, 36 at. % Zn, Table I) was enveloped in  $\beta'$  phase (55 at. % Cu, 44 at. % Zn, Table I). A transverse section of the rod (Figure 2a) was characterized by equiaxed grains ( $\alpha$  and  $\beta'$  phases) with an average size of 24  $\mu\text{m}$  in diameter for the  $\alpha$  phase and 20  $\mu\text{m}$  for the  $\beta'$  phase. Observations of the longitudinal sections of the rod (Figure 2b) showed textured  $\beta'$  grains (their size varied from 20  $\mu\text{m}$  to 120  $\mu\text{m}$  in the longitudinal direction). Moreover,  $\alpha$  grains had preferentially germinated at the  $\beta'$  grain boundaries, leading to a specific chaining of  $\beta'$  and  $\alpha$  phases. Because lead is insoluble in Cu-Zn alloys, lead-rich micro-particles were also observed; they were finely dispersed in the alloy but mainly present at the  $\alpha, \beta'$ -interphases and in the  $\beta'$  phase.

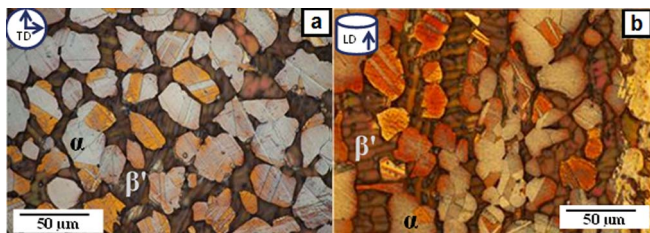


**Figure 2.** Optical microscope observations of the  $\alpha, \beta'$ -brass CuZn40Pb2 (CW617N). The sample was observed after polishing followed by Klemm II etching. (a) transverse section (b) longitudinal section.

**Characterization of the damage after the dissolution tests and determination of dissolution kinetics.**— In all the chosen experimental conditions, on the basis of optical observations, corrosion phenomena were observed essentially in the  $\beta'$  phase, which was more reactive than the  $\alpha$  phase due to the higher amount of Zn, as previously observed.<sup>16</sup> This was in agreement with the results obtained by Assouli et al.<sup>15</sup> who showed that the  $\alpha$  phase, which contains more copper than the  $\beta'$  phase, was more noble than the  $\beta'$  phase. Typical observations of the damage caused by 12 h and 48 h dissolution tests at a constant potential at the reference conditions are presented in Figures 3a and 3b, respectively. A schematic of the corroded zone is presented in Figure 3c. For short tests, the corroded zone was composed of only non-corroded  $\alpha$  grains suggesting a complete dissolution of the  $\beta'$  phase, i.e. both Cu and Zn (and a few alloying elements in the  $\beta'$  phase as Sn and Ni) dissolution from the  $\beta'$  phase. This mechanism was commonly called simultaneous dissolution.<sup>26–28</sup> However, for longer dissolution tests, under the outer-layer composed of only non-corroded  $\alpha$  grains, an inner layer characterized by pink-colored  $\beta'$  grains surrounded by the non-corroded  $\alpha$  phase was observed. Chemical analyses by EDX through the sections of the corroded specimens (Figure 3d) confirmed that the  $\alpha$  phase was not corroded and showed that the  $\beta'$  discoloration was due to a depletion in Zn leading to the formation of a porous Cu-rich phase. In the absence of discoloration, the chemical composition of the  $\beta'$  phase was that of a non-corroded sample. The result highlighted that dezincification of the  $\beta'$  phase in such a leaded  $\alpha, \beta'$ -brass occurred under anodic polarization. Due to the morphology of the corrosion damage, dissolution kinetics were evaluated by measuring two parameters versus the duration of the dissolution tests: the depth of the simultaneous dissolution front, i.e., the average distance between the initial surface of the material and the first  $\beta'$  grain not completely dissolved, and the depth of the dezincification front (i.e., selective dissolution), i.e., the average distance between the initial surface of the material and the first intact  $\beta'$  grain. With such a definition, the depth of the dezincification front included that of the simultaneous dissolution front. The corroded zone was characterized by an elliptical shape (Figures 3a and 3b) corresponding to the  $\beta'$  phase dissolution starting at the edges of the exposed zone that was separated from the protected zone by a varnish (Figure 3c). The depth of the corroded zone was observed to be constant in the center of the exposed zone. Therefore, quantification of the corrosion damage, i.e., measurements of the dissolution depths, by OM observations, were conducted in the center of the exposed zone. The dissolution depth vs. time curves (simultaneous and selective dissolution) for the reference conditions (0.5 M NaNO<sub>3</sub> solution, pH 11, polarization at 0.05 V/SCE without mechanical loading) are presented in Figure 4a. They were characterized by two stages separated by a critical time called  $t_c$ :

- the first stage ( $t < t_c$ ) occurred where the dezincification front merged with the simultaneous dissolution front showing that the corrosion phenomena for the  $\beta'$  phase corresponded to a simultaneous dissolution process. No dezincification of the  $\beta'$  phase was detected under the previously described outer layer;
- the second stage ( $t > t_c$ ) occurred where the dezincification front preceded the dissolution front. At this stage, both the outer layer corresponding to the simultaneous dissolution of the  $\beta'$  phase and the inner layer composed of non-corroded  $\alpha$  grains and the dezincified  $\beta'$  phase were observed. These observations clearly show that during

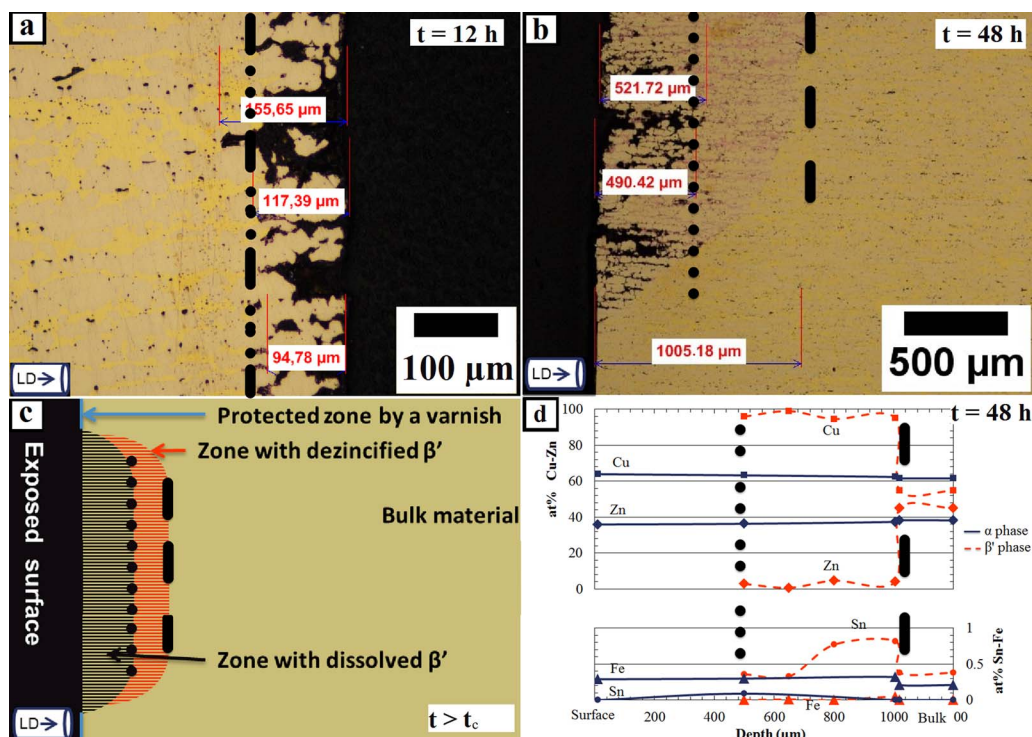


**Figure 3.** Analysis by optical microscope of a section of the  $\alpha, \beta'$ -brass CuZn40Pb2 sample after (a) a 12 h and (b) a 48 h dissolution test in a 0.5 M NaNO<sub>3</sub> solution at pH 11 under anodic polarization at 0.05 V/SCE. (c) Schematic of the corrosion damage and (d) EDX analysis.

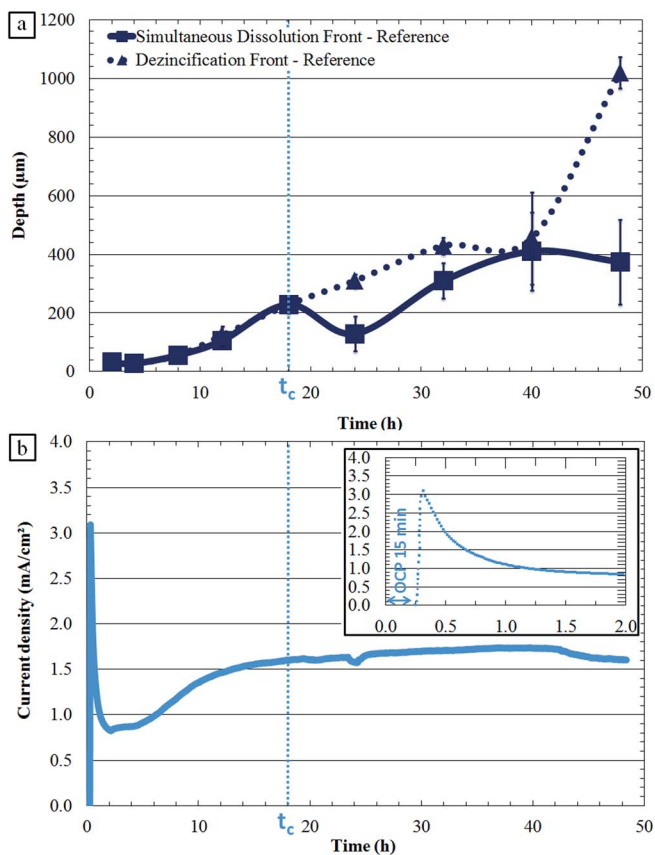


**Figure 4.** (a) dissolution depths (b) current density versus time curve during the dissolution tests of the  $\alpha, \beta'$  brass CuZn40Pb2 for the reference conditions (0.5 M NaNO<sub>3</sub> solution, with a pH adjusted to 11, and an applied potential equal to 0.05 V/SCE; without mechanical loading).

the second stage the simultaneous dissolution of the  $\beta'$  phase had not stopped but continued to proceed with a time lag when compared to the dezincification. When the duration of the dissolution tests increased, the difference in depth between the simultaneous dissolution and dezincification globally increased suggesting that the dezincification extended in depth faster than the simultaneous dissolution. However, due to the difficulty in measuring the dissolution depths, the result was not unambiguously demonstrated in the figures.

Figure 4b shows the current density versus immersion time during the dissolution tests. The curve was characterized, in the first 2 h, by a strong current density peak followed by a quick decrease of the current density. Afterwards, the current density slowly increased or tended to stabilize at approximately 1.7 mA·cm<sup>-2</sup>. Taking into account the uncertainty in the  $t_c$  value, previously evaluated from dissolution curves, it should be assumed that a stable value of the current density was reached for time equal to  $t_c$ . The results showed that the two stages previously defined were clearly observed by recording the current-density versus time. Except for the current peak observed during the first 2 hours, the current density during the second stage was higher than that measured during the first; the stabilization of the current density was probably due to the occurrence, after  $t_c$ , of a dezincification phenomenon along with a simultaneous dissolution. The current peak in the first two hours showed a high rate of dissolution for a few hours followed by a steep fall in current and a slow increase of the current corresponding to a slow increase in the dissolution rate. The current peak in the first two hours was assumed to be due to initiation of dissolution events with the removal of the air-formed film and the formation of a new film on the sample surface. It should be noted also that the air-formed film probably dissolved during the 15 minutes at OCP, before the dissolution tests. Therefore, the results showed that the corrosion damage corresponded to a two-step mechanism: the first step, called as initiation step, was characterized by high current densities and was attributed to  $\beta'$  simultaneous dissolution on the extreme surface. The second step, where the dissolution subsequently went through the material, was called as propagation step. For the initiation

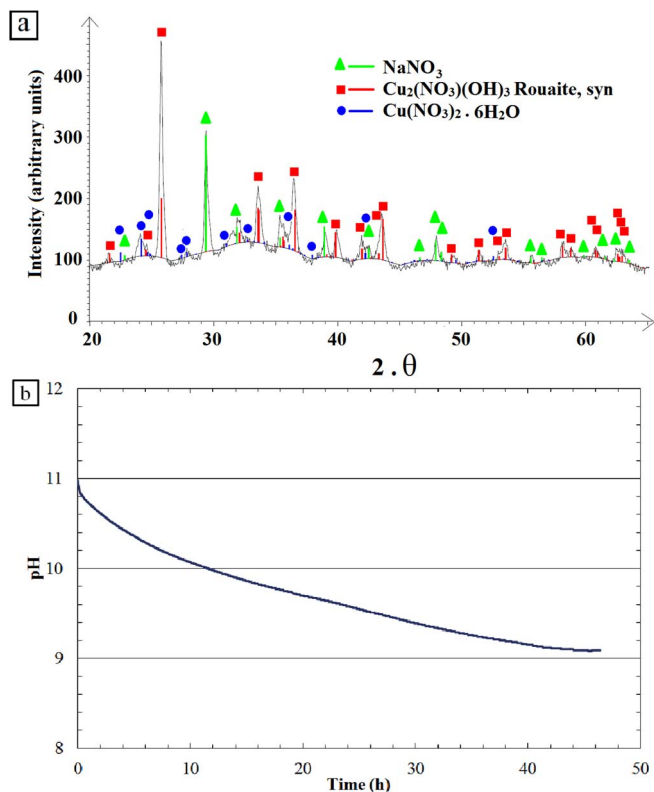


**Figure 5.** (a) XRD analysis of the blue corrosion products (b) pH vs. time during a dissolution test at the reference conditions, i.e., at 0.05 V/SCE in a 0.5 M  $\text{NaNO}_3$  solution at pH 11, without mechanical loading, performed on  $\alpha, \beta'$  brass  $\text{CuZn40Pb2}$ .

step, only simultaneous dissolution of the  $\beta'$  phase (Figure 3a) had to be considered: the dezincification process that probably occurred during the first 15 minutes at the OCP, before the dissolution test, was neglected on the OM observations due to the duration of the shortest tests (2 h). For the propagation step, only simultaneous dissolution of the  $\beta'$  phase was observed before  $t_c$ , while after  $t_c$ , both simultaneous dissolution and dezincification of the  $\beta'$  phase occurred.

*Chemical composition of the electrolyte versus time.*— During dissolution tests at a constant potential, a blue coloring of the solution due to the corrosion products was observed after a delay depending on the stirring of the electrolyte. This could correspond to a change in the aggressiveness of the environment related to the critical time,  $t_c$ , corresponding to the occurrence of a dezincification process. This finding means that the critical time should be correlated with a critical chemical composition of the electrolyte. Therefore, corrosion products in the solution were removed, dried and analyzed by XRD (Figure 5a). These corrosion products were mainly identified as  $\text{Cu}_2(\text{NO}_3)(\text{OH})_3$ , known as rouaite, but there was also evidence of  $\text{Cu}(\text{NO}_3)_2$ . The corrosion products had accumulated on the surface that had been exposed to the electrolyte. In Figure 5b, pH vs. time data points showed a strong decrease of the pH value over time, which could be related to the formation of a very large amount of corrosion products. The cathodic reactions, i.e. oxygen and maybe nitrate reduction, should increase the pH. However, results suggested that this effect was largely compensated by the formation of corrosion products; furthermore, an analysis of the solution showed that nitrate reduction did not occur. Finally,  $\text{CO}_2$  should cause the reduction of the pH because the solution was open to air but experiments performed in deaerated conditions showed that the presence of  $\text{CO}_2$  was not the major parameter to explain the variation of the pH even though this effect could not be excluded.

To understand further the change of the chemical composition of the electrolyte during the dissolution tests, dissolution kinetics were

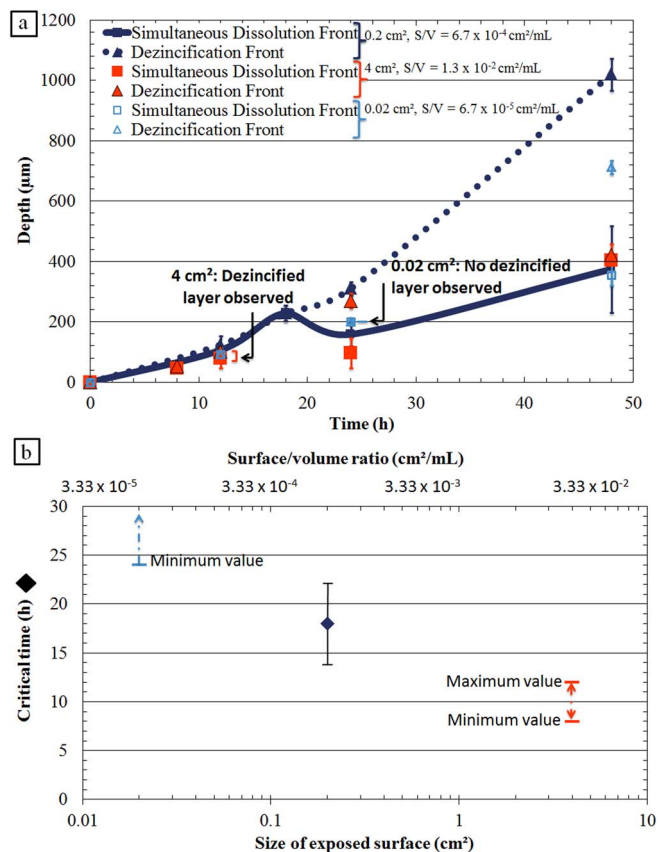


**Figure 6.** (a) Dissolution depths of the  $\alpha, \beta'$  brass  $\text{CuZn40Pb2}$  versus time during the dissolution tests in a 0.5 M  $\text{NaNO}_3$  solution, pH 11, with a potential applied of 0.05 V/SCE, without mechanical loading. All of the measurements were performed for three values of the surface/volume ratio. The ratio  $6.7 \times 10^{-4} \text{ cm}^2/\text{mL}$  corresponded to a surface exposed to  $0.2 \text{ cm}^2$ , i.e., that of the previous experiments; values from Figure 4a were therefore reported for comparison with values obtained for the two other ratios. (b) Critical time  $t_c$  versus the surface/volume ratio.

determined for two additional values of the ratio of the surface exposed to the electrolyte to the volume of the solution (S/V), respectively  $S/V = 6.7 \times 10^{-5} \text{ cm}^2/\text{mL}$  and  $1.3 \times 10^{-2} \text{ cm}^2/\text{mL}$  compared to the ratio used for previous experiments i.e.,  $6.7 \times 10^{-4} \text{ cm}^2/\text{mL}$  (Figure 6). For all the chosen S/V values, two stages were observed on the dissolution depths vs. time curves as described previously (Figure 6a). For  $S/V = 6.7 \times 10^{-5} \text{ cm}^2/\text{mL}$  and  $1.3 \times 10^{-2} \text{ cm}^2/\text{mL}$ , a limited set of experiments was performed. However, for  $S/V = 6.7 \times 10^{-5} \text{ cm}^2/\text{mL}$ , no dezincified layer was observed even after a 24 h dissolution test while dezincification was observed after a 48 h test showing that the minimum value of  $t_c$  would have to lie between 24 h and 48 h. For  $S/V = 1.3 \times 10^{-2} \text{ cm}^2/\text{mL}$ , a dezincified layer was observed after a 12 h dissolution test showing that the maximum value for  $t_c$  was 12 h. Therefore, the results clearly show that an increase in the S/V value shifted the critical time,  $t_c$ , to a lower value, i.e., promoted the occurrence of the dezincification process (Figure 6b). However, mainly for long tests ( $>40 \text{ h}$ ), the dezincification depths were smaller for the large S/V value while the simultaneous dissolution depths were quite similar regardless of the ratio (Figure 6a).

Weight loss measurements on the working electrode ( $\alpha, \beta'$ -brass  $\text{CuZn40Pb2}$  sample) and ICP analyses of the solutions were performed after the dissolution tests for the two higher S/V values, i.e., ratios equal to  $6.7 \times 10^{-4} \text{ cm}^2/\text{mL}$  and  $1.3 \times 10^{-2} \text{ cm}^2/\text{mL}$  (Figure 7 and Figure 8).

Independent of the S/V value, weight loss measurements (Figures 7a and 8a) were coherent with the dissolution depths measured by the OM observations (Figure 6a) with two stage kinetics

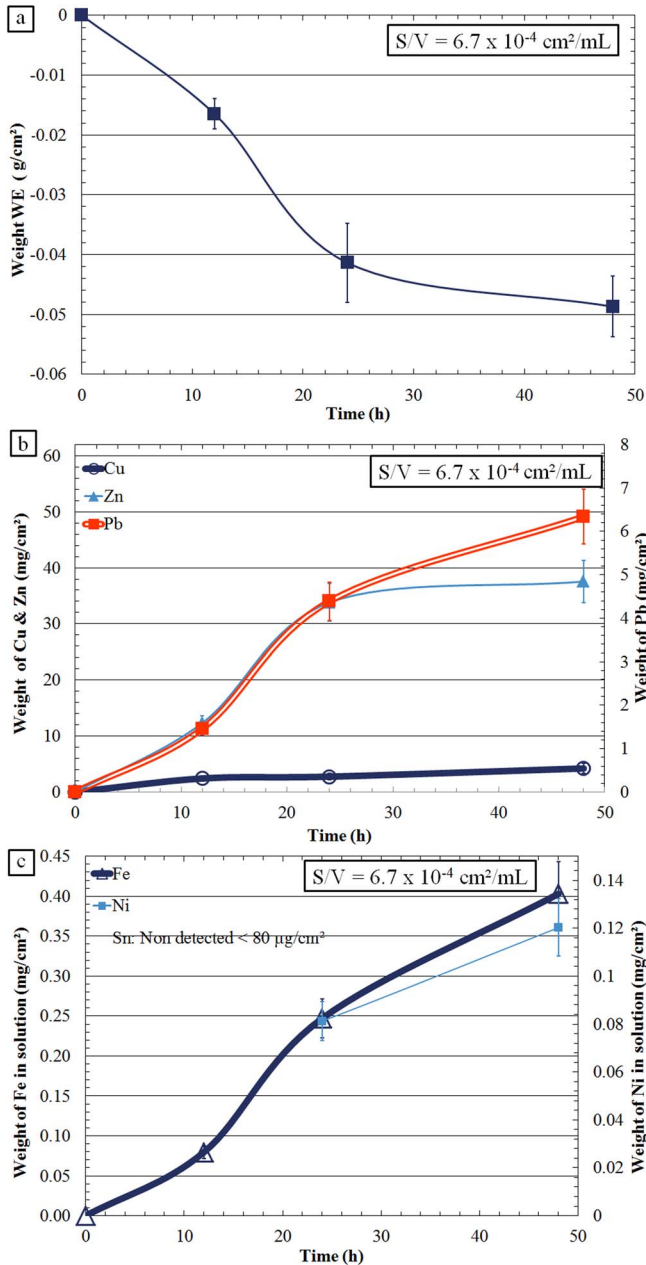


**Figure 7.** (a) Weight loss of the  $\alpha,\beta'$ -brass CuZn40Pb2 sample (b) Cu, Zn and Pb content of the electrolyte (c) concentrations of the impurity elements (Fe, Ni, Sn) of the electrolyte versus time. Results correspond to the reference conditions (0.5 M  $\text{NaNO}_3$  solution, pH 11, potential applied of 0.05 V/SCE, without mechanical loading). The area of the surface exposed was equal to  $0.2 \text{ cm}^2$  for a solution volume of 300 mL ( $S/V = 6.7 \times 10^{-4} \text{ cm}^2/\text{mL}$ ). The alloying element concentration in solution was expressed in  $\text{mg}\cdot\text{cm}^{-2}$  to take into account the size of the surface exposed to the electrolyte.

characterized by a weight loss that rapidly increased in the first stage followed by, after a critical time (quite similar to  $t_c$  measured in Figure 6b), a slowing down of the variation in the weight loss versus time curve in the second stage. Again, during the first stage, simultaneous dissolution of the  $\beta'$  phase occurred, leading to a rapid increase in the weight loss; after the critical time,  $t_c$ , the dezincification occurred and was faster than the simultaneous dissolution, leading to a slowing down of the variation in weight loss. Furthermore, the shift of the critical time  $t_c$  toward lower values when the  $S/V$  ratio increased was observed by comparing the weight loss curves plotted for the two  $S/V$  values (Figures 7a and 8a), which is in agreement with Figure 6b.

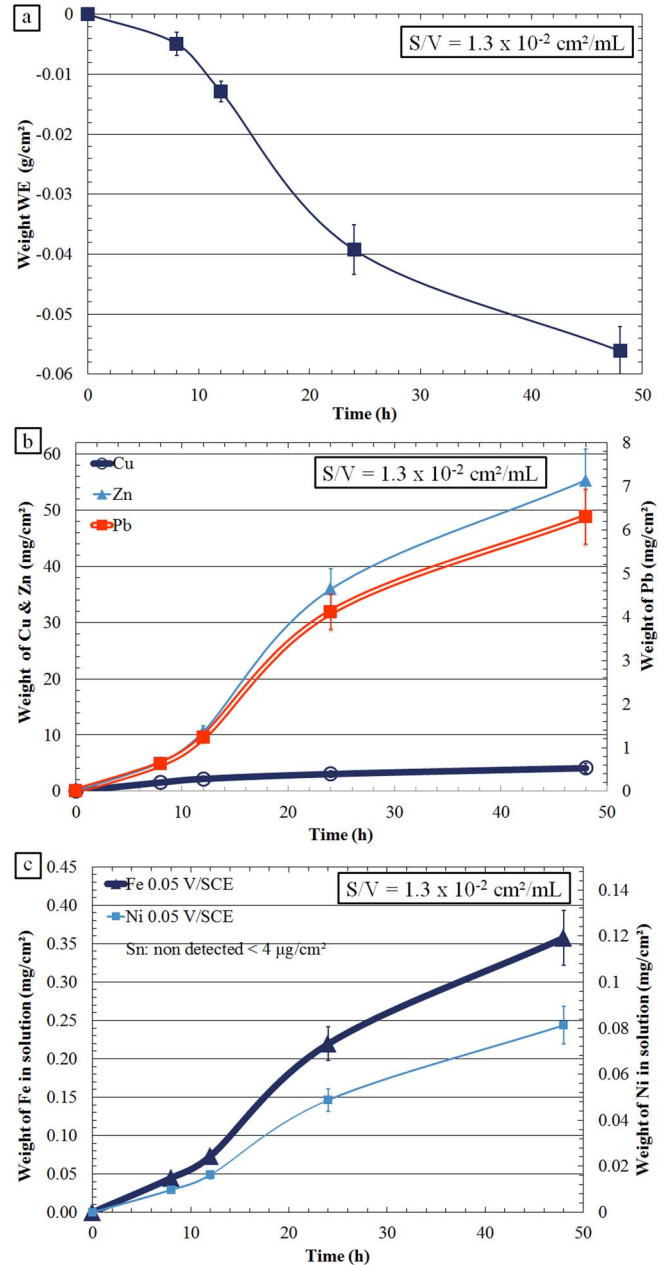


**Figure 8.** (a) Weight loss of the  $\alpha,\beta'$ -brass CuZn40Pb2 sample (b) Cu, Zn and Pb concentrations of the electrolyte (c) concentrations of the impurity elements (Fe, Ni, Sn) of the electrolyte versus time. Results correspond to the reference conditions (0.5 M  $\text{NaNO}_3$  solution, pH 11, potential applied of 0.05 V/SCE, without mechanical loading). The area of the surface exposed was equal to  $4 \text{ cm}^2$  for a solution volume of 300 mL ( $S/V = 1.3 \times 10^{-2} \text{ cm}^2/\text{mL}$ ). The alloying element concentration in solution was expressed in  $\text{mg}\cdot\text{cm}^{-2}$  to consider the size of the surface exposed to the electrolyte.

Figures 7b and 8b show the Cu and Zn content in the electrolyte versus time. Regardless of the duration time of the dissolution tests or the  $S/V$  ratio, the amount of zinc inside the solution was higher than that of copper, but the differences in the amounts of the two elements were significantly increased during the second stage. This was consistent with the dissolution mechanisms. For short times, before  $t_c$ , a simultaneous dissolution of the  $\beta'$  phase occurred. Due to the chemical composition of the  $\beta'$  phase (55 at.% Cu and 44 at.% Zn), the Cu and Zn amounts in solution should be similar. If the errors on the measurements were neglected, the differences could be explained by the precipitation of Cu-rich species that had not been dissolved and

were lost during the preparation of the solution for the ICP analyses (see experimental part). For longer times, after  $t_c$ , the strong increase of the amount of Zn compared to Cu corroborated the occurrence of a dezincification process that was faster than the simultaneous dissolution. Furthermore, a close-up on the Cu versus time curves showed that the rate of leaching of Cu decreased near the critical time, while the amount of Zn continued to increase for longer times during the dissolution tests. This suggested that the transition from the first stage to the second stage is related to the amount of Cu in solution that can be correlated to the accumulation of Cu-rich products on the brass. The weight loss and the amount of the major elements dissolved (by surface unit) for the different S/V experiments did not reflect the difference observed in the kinetics with the different dissolution depths. However, as suggested before, a certain amount of the corrosion products probably remained on the brass sample and had not been taken into account during the ICP analyses.

Results concerning the impurity elements (Figures 7c and 8c), mainly Fe that had segregated in the  $\alpha$  phase and potentially at the interphases, suggested that, even if the corrosion damage was localized on the  $\beta'$  phase, the  $\alpha$  phase surface might be slightly dissolved. However, the Fe amount was very low and, as explained previously, corrosion phenomena on  $\alpha$  phase was considered as negligible. Finally, Figures 7b and 8b showed that Pb ions were also leached into the solution. The influence of the S/V ratio on the extent of leaching of Pb could not be evaluated but, for the two S/V values, the amount of Pb leached into the solution strongly increased after the critical time  $t_c$ .

#### *Influence of a mechanical loading on the dissolution kinetics.*—

Figure 9 shows the effects of mechanical loading on the dissolution processes. Depths of both dissolution processes vs. time curves without mechanical loading were reported for comparison. It is worth noting that new reference curves were plotted with samples placed on the bending device without applying a mechanical loading to eliminate the effects of the bending device, because, due to the geometry of the bending device, local electrochemical conditions could be different between experiments performed with and without the bending device even though the global surface/volume ratio was the same for experiments using the bending device and others without this device. The bending device corresponded to a cell open to the bulk but, due to the limited volume between the cell and the sample, an evolution of the solution inside the cell could not be excluded. Furthermore, stirring conditions inside the cell could be different than outside. Finally, the local conditions could vary between the tensile and the compressive surfaces. This explained the differences in the reference curves in comparison to those plotted in Figure 4a. In particular, comparison of the curves plotted without the bending device (Figure 4a) and that with the bending device for the tensile surface without applying a mechanical loading (Figure 9a), showed that the use of the bending device induced a delay in the emergence of the dezincification front. On the other side corresponding to the compressive surface, comparison of Figures 4a and 9b showed that the use of the bending device did not change the critical time for the reference conditions, i.e. without mechanical loading. However, because the dissolution depths versus time curves were plotted for the reference conditions without a mechanical load though using the same device, it was possible to draw conclusions about the effects of the mechanical loading on the dissolution kinetics. The results clearly showed that all curves exhibited two stages, as previously explained, with a first stage where the dezincification front merged with the simultaneous dissolution front and, after  $t_c$ , a second stage where both simultaneous dissolution and dezincification of the  $\beta'$  phase occurred, dezincification extending faster in depth than the simultaneous dissolution. Due to the previous comments concerning the bending device geometry, there was no comparison of the critical times measured for the tensile and compressive surfaces. Major results were that (i) there was no effect of a tensile mechanical loading on the critical time compared to samples without a mechanical loading; the simultaneous dissolution front was not significantly affected during the entire dissolution test

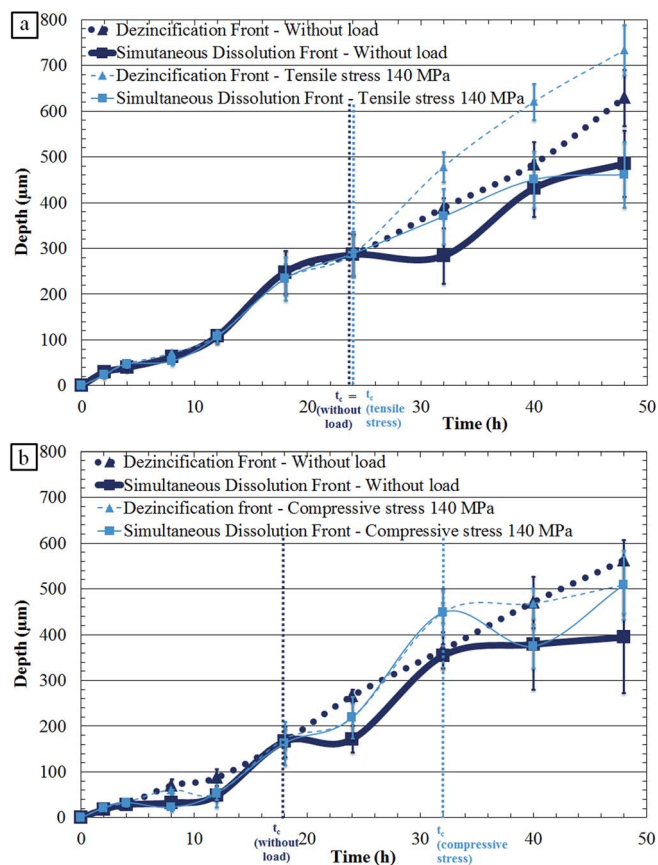


**Figure 9.** Influence of (a) tensile and (b) compressive mechanical loading on the depth of the dissolution of the  $\alpha,\beta'$ -brass CuZn40Pb2. In each graph, the effect of the mechanical loading is studied in comparison with the results obtained for the reference conditions (0.5 M NaNO<sub>3</sub>, pH 11, applied potential equal to 0.05 V/SCE without mechanical loading).

by the loading but, under tensile mechanical loading, during the second stage, i.e. after  $t_c$ , the dezincification front progress was faster by comparison to the reference conditions without mechanical loading (Figure 9a) (ii) under compressive mechanical loading, the critical time was significantly increased compared to the results without mechanical loading (Figure 9b). However, the kinetics of both dissolution processes were in the range of those measured without mechanical loading.

## Discussion

*Dissolution mechanisms of the  $\alpha,\beta'$ -brass CuZn40Pb2 in nitrate solution.*— The results (Figure 4) showed that the corrosion behavior of the  $\alpha,\beta'$ -brass CuZn40Pb2 in nitrate solution, under anodic polarization, for long immersion times was described by a two-step mechanism including an initiation step followed by a propagation step.

Concerning the initiation step, the high rate of dissolution in the early stages (current density peak) of the dissolution tests was related to initiation of dissolution events as previously stated, and in agreement with literature data.<sup>31</sup> During the first 15 minutes at OCP before the potential was applied for the dissolution tests, dezincification should occur on the sample surface, due to the high Zn amount in the brass and the galvanic coupling between the  $\alpha$  and  $\beta'$  phases, as shown in previous work.<sup>16</sup> However, due to the short time at OCP, this phenomenon only concerned the extreme surface layer and only simultaneous dissolution was observed using optical observations during the initiation step of the dissolution tests. Indeed, during immersion at OCP before the dissolution tests, dissolution processes led to the



formation of a passive film mainly composed of  $\text{Cu}_2\text{O}$  with a very low amount of  $\text{ZnO}$ .<sup>16</sup> When the anodic potential was applied for the dissolution tests, evolution of the oxide layer should occur but copper oxides remained present. The influence of lead was also suspected to be strong with the incorporation of lead in to the passive layer, due to the dissolution of Pb particles, which improved the corrosion resistance.<sup>16,20,24,25</sup> Kumar et al. showed that a high amount of lead in brass could provide an improvement in corrosion resistance under conditions where compounds of lead were precipitated on the surface.<sup>24</sup> The equilibrium of the electrolyte with this  $\text{Cu}_2\text{O}$  and lead oxides-rich film made it difficult to initiate dezincification as suggested by different authors.<sup>26–34</sup> This was in agreement with low dissolution depths for the two first hours and the decay of the current density observed on the current density versus time (Figure 4b) after the initial peak.

After 2 h, the dissolution extended in depth which initiated the propagation step of the dissolution tests, but before  $t_c$ , only simultaneous dissolution of the  $\beta'$  phase occurred. This was in agreement with the corrosion behavior described by Pickering and Kim<sup>27</sup> concerning an alloy susceptible to dealloying. They showed that, initially, selective dissolution could occur and one of three phenomena then happened. The dissolution rate could decrease due to the protective nature of the modified surface layer. The planar surface could become unstable and local penetration could occur, or the dealloying could stop and give way to a non-selective reaction of the alloy.<sup>27</sup> The last phenomenon could happen when the alloy was exposed to conditions which did not produce a protective surface layer. In the present case, it was assumed that when a sufficient drop in the pH value was achieved at the surface (Figure 5b), a part of the hydroxide (rouaite) that was formed, dissolved. In more general terms, the modification of the surface layer should correspond to the formation of non-protective reaction-product layers which would lead to an increase in the simultaneous dissolution kinetics after 2 h. The question that remains is why, after  $t_c$ , dezincification, i.e., selective dissolution of the  $\beta'$  phase, occurred. Sieradzki et al. proposed a percolation mechanism of dealloying based on the concept that above a critical concentration there exist continuous atomic scale conduits of the more reactive component allowing selective dissolution to happen.<sup>31–34</sup> It could be assumed here that, due to the simultaneous dissolution processes that had occurred for  $\beta'$  phase before  $t_c$ , the percolation threshold had been reached. Furthermore, Sieradzki et al. showed that the transition from simultaneous dissolution to selective dissolution corresponded to the growth of a macroscopic three-dimensional dealloyed structure which defined a roughening transition with a competition between dissolution of the more active component leading to surface roughening and the curvature-driven surface diffusion of the more noble component.<sup>31–34</sup> It is clear that the dissolution of an atom depends not only on the number of nearest neighbors in the metal but also on their identity, and therefore to the alloy composition. Again, the simultaneous dissolution of  $\beta'$  phase before  $t_c$  should generate a local atomic environment conducive to a stronger reactivity for the more reactive component, i.e. Zn. Furthermore, the propensity to dissolution for an element depends also on the electrolyte composition. Therefore, the transition from simultaneous dissolution to dezincification could also be correlated to further modification of the chemical composition of the electrolyte (Figure 5b). The local dissolution phenomena observed before  $t_c$ , with simultaneous dissolution of the  $\beta'$  phase while the  $\alpha$  phase remained uncorroded, should generate an increase in the surface roughness, at a macroscopic scale, with the formation of cavities between the uncorroded  $\alpha$  grains. The duration of the simultaneous dissolution process should correspond to the time needed for the electrolyte trapped inside the cavities to reach a critical composition corresponding to the destabilization of  $\beta'$  surface. This was consistent with the extent of leaching of Pb before  $t_c$  when the duration of the tests increased. After  $t_c$ , the share of Pb in the oxidized metal leached from or accumulated on the surface, was more evenly disturbed as evidenced by the strong increase in the amount of Pb leached in after  $t_c$  (Figures 7b and 8b), because of the removing of Pb particles due to increased  $\beta'$  phase dissolution.

Therefore, the results suggested that once the process of dissolution was initiated, any change in the chemical composition of the electrolyte was one of the most obvious parameters that could explain the variations observed in the general rate of dissolution, as well as the occurrence of the dezincification process. In particular, previous studies in the literature demonstrated the major role of the copper concentration in solution on the transition between the simultaneous dissolution and dezincification of the Cu/Zn elements.<sup>35</sup> Sieradzki et al. showed that severe dezincification occurred in concentrated chloride solutions where cuprous ions were highly stabilized by complexing, when compared with cupric ions.<sup>31</sup> Therefore, the Cu concentration in solution, i.e., a solubility limit achievement for Cu, remained a relevant parameter that should explain the transition at  $t_c$  between the two stages. The transition at  $t_c$  from the first stage, with the simultaneous dissolution of only the  $\beta'$  phase, to the second stage, with Zn dezincification of the  $\beta'$  phase faster than the simultaneous dissolution, was identified for each of the experiments performed using a different S/V ratio which corresponded with different Cu and Zn concentrations in solution. Results showed that the dezincification front was observed for:

- $[\text{Cu}] = 7 \text{ mg} / 300 \text{ mL} = 5.9 \text{ mg} \cdot \text{cm}^{-2} \cdot \text{L}^{-1}$   $[\text{Zn}] = 30 \text{ mg} / 300 \text{ mL} = 25 \text{ mg} \cdot \text{cm}^{-2} \cdot \text{L}^{-1}$  for a  $4 \text{ cm}^2$  exposed surface
- $[\text{Cu}] = 0.5 \text{ mg} / 300 \text{ mL} = 8.3 \text{ mg} \cdot \text{cm}^{-2} \cdot \text{L}^{-1}$   $[\text{Zn}] = 5 \text{ mg} / 300 \text{ mL} = 83.3 \text{ mg} \cdot \text{cm}^{-2} \cdot \text{L}^{-1}$  for a  $0.2 \text{ cm}^2$  exposed surface

Taking into account the inherent errors of the chemical analysis and the lack of accuracy for the  $t_c$  values determined from the dissolution depths vs. time curves, the results showed that a critical concentration of Cu in solution per area of exposed material for a particular potential could be identified as a way to explain the transition between the two stages with the separation of both of the dissolution fronts: it was approximately  $6\text{--}8 \text{ mg} \cdot \text{cm}^{-2} \cdot \text{L}^{-1}$  for the reference conditions. It might have a different value for other experimental conditions (another pH, another nitrate concentration or another applied potential) because these parameters also influenced the stability of the oxide layers and corrosion products and the dissolution kinetics of the more active component, i.e. Zn.

*Influence of the mechanical loading on the dissolution kinetics.*— The objective is to understand the influence of the mechanical loading on the progress of the dezincification throughout the material. According to Sieradzki,<sup>30–34</sup> dezincification proceeds with a percolation dissolution mechanism which is first characterized by the formation of connected clusters of the more reactive components, i.e. Zn, in the bulk and these percolating clusters of atoms provide a continuous active path for the dissolution process. Further, they provide pathways for the electrolyte to enter the bulk solid by dissolving Zn. Regarding the high Zn proportion in the  $\beta'$  phase, the density of these paths inside the  $\beta'$  phase after dezincification should be considered strong. According to the literature, it was demonstrated that dezincification induced a tensile stress in the dezincification layer of brass.<sup>21,36–37</sup> For the  $\beta'$ -phase in  $\alpha$ - $\beta'$  brass, the stress level could be high enough to influence strongly the morphology of the previous paths. They could be very large, and after dissolution they could lead to the formation of pores with a high degree of percolation, i.e. features like tunnels in contact with the electrolyte trapped between the non-corroded  $\alpha$  grains. Such a morphology of the porous structure is in good agreement with Sieradzki's observations.<sup>34</sup> The lead particles in the dezincified layer could contribute to this high degree of percolation, in being dissolved or in decreasing the mechanical properties of the dezincified layer while dezincification induced stress. A schematic of the proposed mechanism is shown in Figure 10. Such a mechanism should be in good agreement with the results obtained concerning the influence of the mechanical loading (Figure 9). At a macroscopic scale, the mechanical loading, by inducing a strain in the alloy, should influence the shape of the "tunnels". A compressive mechanical loading should promote the closing of the "tunnels", so that they did not contain enough free volume for the electrolyte to penetrate the evolving porous structure.

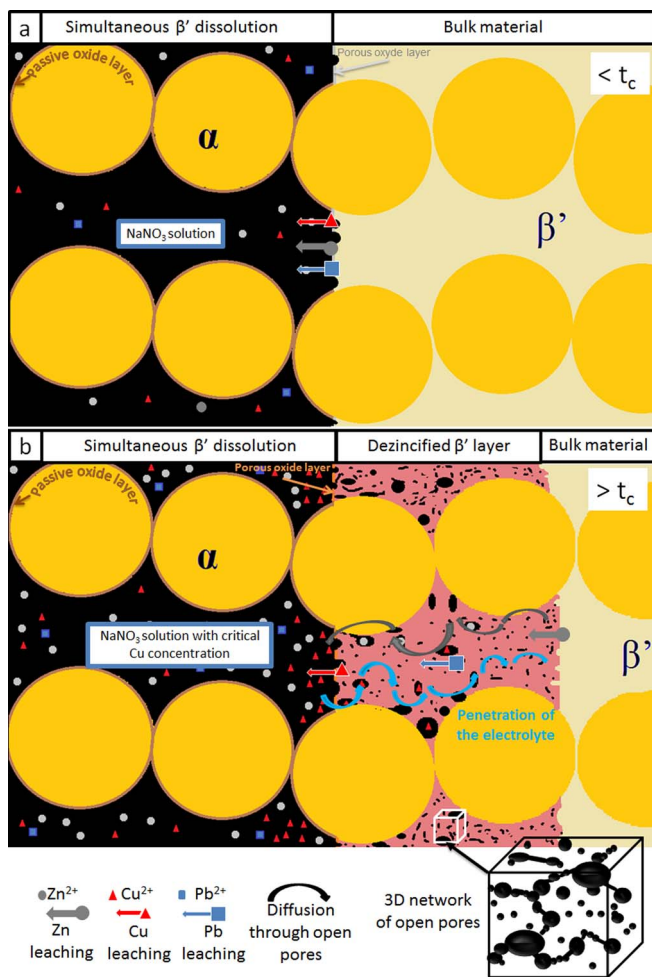


**Figure 10.** Schematic of the proposed dezincification mechanism (a) before  $t_c$  (b) after  $t_c$ .

Therefore, a compressive loading was expected to delay the dezincification of the  $\beta'$  phase which was in agreement with Figure 9b;  $t_c$  was shifted toward longer times showing that a compressive mechanical loading promoted the simultaneous dissolution to the detriment of dezincification. On the contrary, a mechanical tensile loading should contribute to opening the “tunnels”. Therefore, this loading was expected to accelerate the dezincification kinetics as shown in Figure 9a. Furthermore, the mechanical loading should influence the dissolution behavior of the  $\alpha$ - $\beta'$  brass at an atomic scale. Indeed, as previously stated, the dissolution potential of an atom depends not only on its chemical environment (number and identity of its neighbors) but also on the local stress state. Therefore, mechanical loading should also influence the roughening transition, thereby explaining the transition from simultaneous dissolution to dezincification.

### Conclusions

Results for the  $\alpha$ , $\beta'$ -brass CuZn40Pb2 in NaNO<sub>3</sub> solutions are summarized in the following points.

- Dissolution tests, in a 0.5 M NaNO<sub>3</sub> solution, at pH 11, at a constant anodic potential, led to the dissolution of the  $\beta'$  phase while the  $\alpha$  phase remained uncorroded.
- The corrosion behavior of the  $\alpha$ , $\beta'$ -brass was characterized by a two-step mechanism: (i) an initiation step for which simultaneous dissolution of only the  $\beta'$  phase occurred; (ii) a propagation step,

including simultaneous dissolution, before a critical time  $t_c$ , and both, simultaneous dissolution and dezincification of the  $\beta'$  phase, after  $t_c$ .

- The results were in good agreement with the percolation dissolution mechanism proposed by Sieradzki et al.<sup>30-34</sup> A critical composition of the electrolyte, i.e., a critical concentration of copper per area of exposed material, correlated with a pH value, at the bottom of the corrosion damage contributed to explain the transition from simultaneous dissolution of the  $\beta'$  phase to dezincification. The dezincification led to the development of a porous structure, having a high degree of percolation. The electrolyte could penetrate inside these “tunnels” allowing the corrosion process to continue.

- Depending on its sign (tensile or compressive stress), a mechanical loading could close or open the “tunnels” thereby significantly affecting the kinetics of the  $\beta'$  phase dezincification.

### Acknowledgments

The authors express their sincere thanks to J-C. Salabura for the design of the bending device utilized in the study and R. Mainguy for providing the technical support to establish the experimental device.

This work was performed in the framework of the CETIMAT. The CIRIMAT and the CETIM collaborate for certain aspects of their research activities; this collaboration is performed in a joint laboratory, called CETIMAT.

### References

1. K. Sieradzki, J. S. Kim, A. T. Cole, and R. C. Newman, *J. Electrochem. Soc.*, **134**(7), 1635 (1987).
2. J. Yu and R. N. Parkins, *Corros. Sci.*, **27**(2), 159 (1987).
3. J. Yu, R. N. Parkins, Y. Xu, G. Thompson, and G. C. Wood, *Corros. Sci.*, **27**(2), 141 (1987).
4. R. B. Rebak, R. M. Carranza, and J. R. Galvele, *Corros. Sci.*, **28**(11), 1089 (1988).
5. A. T. Cole, R. C. Newman, and K. Sieradzki, *Corros. Sci.*, **28**(1), 109 (1988).
6. R. M. Carranza and J. R. Galvele, *Corros. Sci.*, **28**(9), 851 (1988).
7. D. Wu, H. S. Ahluwalia, H. Cai, J. T. Evans, and R. N. Parkins, *Corros. Sci.*, **32**(7), 769 (1991).
8. F. Mackay, J. T. Evans, and R. N. Parkins, *Corros. Sci.*, **33**(5), 699 (1992).
9. E. A. Ashour and B. G. Ateya, *Corros. Sci.*, **37**(3), 371 (1995).
10. M. G. Alvarez, P. Lapitz, S. A. Fernandez, and J. R. Galvele, *Corros. Sci.*, **47**, 1643 (2005).
11. P. Lapitz, J. Ruzzante, and M. G. Alvarez, *Corros. Sci.*, **49**(10), 3812 (2007).
12. M. B. Hintz, L. J. Nettleton, and L. A. Heldt, *Metall. Trans. A*, **16A**, 971 (1985).
13. M. B. Hintz, W. K. Blanchard, P. K. Brindley, and L. A. Heldt, *Metall. Trans. A*, **17A**, 1081 (1986).
14. F. Zucchi, G. Trabanelli, M. Fonsati, and A. Giusti, *Mater. Corros.*, **49**, 864 (1998).
15. B. Assouli, A. Srhiri, and H. Idrissi, *NDT&E Int.*, **36**, 117 (2003).
16. C. Berne, E. Andrieu, J. Reby, J-M. Sobrino, and C. Blanc, *J. Electrochem. Soc.*, **162**(12), C648 (2015).
17. E. Brandl, R. Malke, T. Beck, A. Wanner, and T. Hack, *Mat. Corros.*, **60**(4) (2009).
18. E. Sarver and M. Edwards, *Corros. Sci.*, **53**, 1913 (2011).
19. C. Mapelli, D. Mombelli, S. Barella, and A. Gruttadauria, *Eng. Fail. Anal.*, **27**, 141 (2013).
20. S. A. Fernandez and M. G. Alvarez, *Corros. Sci.*, **53**, 82 (2011).
21. J. J. Podesta, G. P. Rothwell, and T. P. Hoar, *Corros. Sci.*, **11**, 241 (1971).
22. L. Burzynska, *Corros. Sci.*, **43**, 1053 (2001).
23. R. H. Heidersbach and E. D. Verink, *Corrosion*, **28**, 397 (1972).
24. S. Kumar, T. S. N. Sankara Narayanan, A. Manimaran, and M. Suresh Kumar, *Mater. Chem. Phys.*, **106**, 134 (2007).
25. G. V. Korshin, J. F. Ferguson, and A. N. Lancaster, *Corros. Sci.*, **42**, 53 (2000).
26. H. W. Pickering and C. Wagner, *J. Electrochem. Soc.*, **114**(7), 698 (1967).
27. H. W. Pickering and Y. S. Kim, *Corros. Sci.*, **22**(7), 621 (1982).
28. H. W. Pickering, *Corros. Sci.*, **23**(10), 1107 (1983).
29. A. P. Pchel'nikov, A. D. Sitnikov, A. K. Marshakov, and V. V. Losev, *Electrochim. Acta*, **26**(5), 591 (1981).
30. K. Wagner, S. R. Brankovic, N. Dimitrov, and K. Sieradzki, *J. Electrochem. Soc.*, **144**(10), 3545 (1997).
31. R. C. Newman, T. Shahrabi, and K. Sieradzki, *Corros. Sci.*, **28**(9), 873 (1988).
32. K. Sieradzki, N. Dimitrov, D. Movrin, C. McCall, N. Vasiljevic, and J. Erlebacher, *J. Electrochem. Soc.*, **149**(8), B370 (2002).
33. K. Sieradzki, *J. Electrochem. Soc.*, **140**(10), 2868 (1993).
34. Q. Chen and K. Sieradzki, *J. Electrochem. Soc.*, **160**(6), C226 (2013).
35. A. V. Polunin, A. P. Pchel'nikov, V. V. Losev, and I. K. Marshakov, *Electrochim. Acta*, **27**(4), 467 (1982).
36. H. Lu, K. Gao, and W. Chu, *Corros. Sci.*, **40**(10), 1663 (1998).
37. X. J. Guo, K. W. Gao, L. J. Qiao, and W. Y. Chu, *Corros. Sci.*, **44**, 2367 (2002).